THE JOURNAL OF PHYSICAL CHEMISTRY C
A JOURNAL OF THE AMERICAN CHEMICAL SOCIETY

pubs.acs.org/JPCC

Article

Molecular Simulation of Biobutanol Recovery Using LTA and CHA Zeolite Nanosheets with an External Surface

Alechania Misturini, Fernando Rey, and German Sastre*

Cite This: J. Phys. Chem. C 2022, 126, 17680−17691

Read Online

ACCESS | Metrics & More | Article Recommendations | Supporting Information

ABSTRACT: LTA and CHA zeolites with silica and silico-aluminophosphate (SAPO) composition have been recently proposed by Van der Perre et al. (*ChemSusChem***2017**,*10,* 2968) to recover butanol from a mixture of butanol, ethanol, acetone, and water. Such a mixture is obtained from biomass fermentation, which is a sustainable alternative for butanol production. Here, we establish a computational methodology to simulate the three-step process, consisting of selective adsorption of butanol, with some ethanol and water, from the initial mixture, using a silica LTA nanosheet; desorption of the adsorbed mixture by increasing the temperature; and adsorption of the desorbed products in a CHA (silica or SAPO) nanosheet. A combination of Monte Carlo simulations, allowing to reproduce or predict single- or multiple-component gas adsorption isotherms, and molecular dynamics, giving the time evolution of the selective adsorption and desorption processes, have been used to model the experimental setup. A recently parameterized force field of general use for zeolites, AlPOs, and SAPOs has been tuned up in order to describe all interactions arising from this model, allowing to capture the thermodynamics of the system, the flexibility of the frameworks, and the effects of surface and bulk in the permeability of the nanosheets.

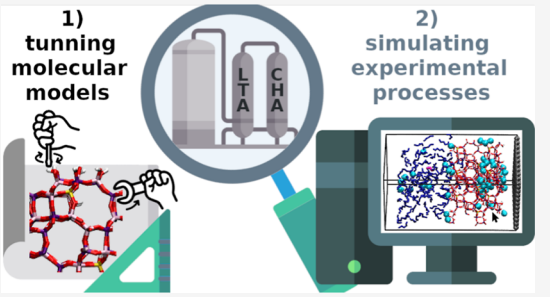

1. INTRODUCTION

The use of biofuels can be a sustainable option for the world's growing energy demand. For instance, biobutanol (1-butanol, also known as biogasoline) can be used by the actual engines without modifications and possess approximately 85% of the energy content in gasoline, besides other advantages.[2] Through the ABE (acetone, butanol, and ethanol) fermentation process, biobutanol can be obtained from biomass.[1] This fermentation of renewable feedstocks by anaerobic bacteria produces a mixture with a ratio of 3 acetone/6 butanol/1 ethanol, diluted in water.[3] The following separation and purification of the produced biobutanol can be done by adsorptive methods, requiring significantly less energy than distillations.[4] In this sense, zeolites present a wide variety of structures, where the microporosity and chemical composition can be tuned for highly selective adsorptions and separations. Experimental and computational studies employing zeolitic materials for the separation of ABE fermented mixture have been reported, analyzing the performance of pure silica and aluminosilicate zeolites with MFI,[5−12] BEA,[5,6,13] FAU,[6] MEL,[11] and CHA[14] topologies, as well as the ZIF-8[15,16] metal−organic framework. Material hydrophobicity has been highlighted as an important aspect for the selective adsorption of butanol from the fermented aqueous mixture.[1,6,10] Besides, various experimental setups have been designed, such as the adsorption−drying−desorption process for recovering butanol from water with silicalite pellets[8] as well as membranes of silicalite-1 (MFI) supported on Al-free yttria-stabilized zirconia substrates, which presented high selectivity to ethanol in aqueous media[7] and high performance for separation of ABE fermented solution at low temperature,[12] and also the combination of frameworks with complementary selectivity, such as ZIF-8 and SAPO-34,[15] or LTA and SAPO-34.[1] The effect of CO_2 in the recovery of biobutanol from the fermented broth by silica LTA and ZIF-8 hydrophobic adsorbents was also investigated experimentally and computationally.[16]

In the selective adsorption process proposed by Denayer and co-workers,[1] the hydrophobicity and affinity of LTA for butanol are combined with the high affinity of SAPO-34 for water and ethanol, allowing butanol recovery with high purity. This experimental procedure involves butanol separation from the fermented mixture vapor phase, followed by its purification. It is performed in tree steps, as illustrated by Figure 1, and three main processes occurs in the columns: (A) first, the fermented vapor phase (mixture containing acetone, butanol, ethanol, and water) passes through an ITQ-29 (pure silica LTA) column at 313 K (during step 1, Figure 1). Butanol and small amounts of ethanol and water are adsorbed by ITQ-29,

Received: June 22, 2022
Revised: September 30, 2022
Published: October 11, 2022

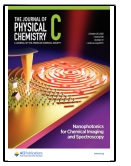

https://doi.org/10.1021/acs.jpcc.2c04331
J. Phys. Chem. C 2022, 126, 17680−17691

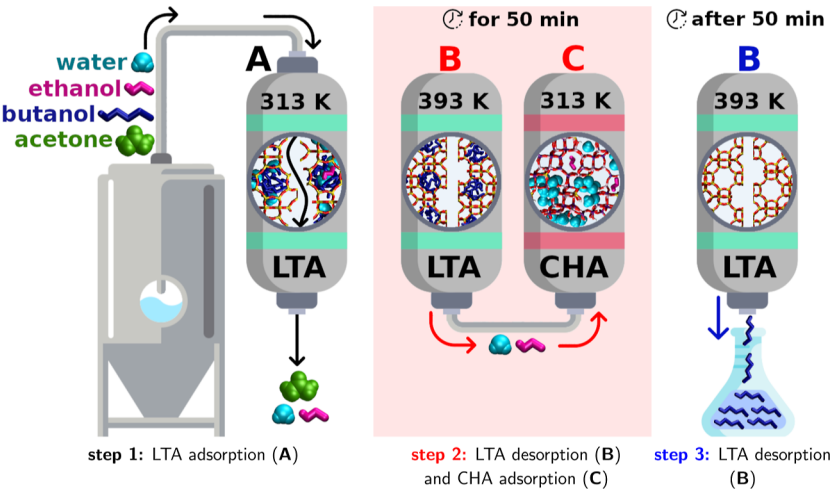

Figure 1. Scheme of the experimental setup for biobutanol recovery designed by Denayer et al.,[1] illustrating the processes (A–C) that occur in each step.

while acetone and remaining ethanol and water molecules flow through the column, being discarded. The acetone fraction present in the vapor mixture is excluded by size from both employed zeolites as their 8-ring dimensions (4.2 × 4.2 Å for LTA and 3.8 × 4.2 Å for CHA) are smaller than the acetone kinetic diameter (4.7 Å);[1] (B) second, the temperature of the ITQ-29 column is increased (393 K) to promote the desorption of its adsorbed content. During the first 50 min (step 2, Figure 1), ITQ-29 mainly desorbs ethanol and water. (C) The above desorbed gases are redirected by a stripping gas toward a CHA column (either silicate or silico-aluminophosphate, SAPO, called, respectively, SSZ-13 and SAPO-34), which operates at 313 K (also during step 2, Figure 1). Although SSZ-13 is not pure silica, albeit of a high Si/Al ratio,[17] its name is usually employed, by extension and in the absence of a specific name, as a synonym of pure silica CHA. As confirmed by breakthrough experiments,[1] ethanol and water are first desorbed from ITQ-29 and become adsorbed by the CHA material, while butanol remains adsorbed in ITQ-29. After 50 min of CHA column operation, this second column is disconnected from the system, and the desorbed content from ITQ-29 is butanol of high purity (step 3, Figure 1).

A computational simulation of this process is very convenient in order to try to improve this and other similar processes by, for instance, testing the effect of using a large variety of other zeolite topologies as well as chemical compositions, Si/Al ratios in aluminosilicate zeolites, or Si/(Si + Al + P) content in SAPOs. In the future other effects such as the morphology and thickness of the crystals can be introduced as important variables to fine tune the process. By having performed a detailed experimental study,[1] it is possible to benchmark our computational methodology and models. This methodology could be employed in order to design and simulate other related chemical engineering processes with separation purposes. Previous studies have assessed the suitability of materials for separation by only taking into account bulk models,[18−23] although an increasing number of studies also include the effect of the external surface[24−26] and crystal morphology,[27,28] as well as crystal thickness.[29,30]

In this study, we try to move along with recent studies, introducing sophisticated models resembling the experimental columns or nanosheets and also taking into account the engineering aspects such as the presence of three differentiated steps in the separation process, involving adsorption/desorption cycles, with different temperatures and materials. This requires not only an updated force field but also a unified approach for the Monte Carlo and molecular dynamics (MD) calculations, which are usually made in the literature using different force fields. For instance, adsorption isotherms will be calculated in the present study in order to find the equilibrium mixture of adsorbed butane, ethane, and water in pure silica LTA. Various models will be compared with the experimental pure component adsorption isotherms,[1] and the best model will be employed for the calculation of the mixture adsorption isotherms, considering the experimental ratio of butanol, ethanol, and water in the fermented vapor phase. The corresponding system at equilibrium (process A) should then be calculated using MD in order to find whether the kinetics corresponding to the second process (B, desorption of the adsorbed mixture at equilibrium) leads to a selective desorption of ethanol and water while butanol remains adsorbed. Also, the diffusion and preferential adsorption of desorbed ethanol and water molecules in the CHA material (process C) can be simulated with MD, where adsorbate affinity and dynamics in the zeolite or SAPO material can be further analyzed. MC and MD calculations employ different zeolite···adsorbate force fields because diffusivity of adsorbates cannot be accurately reproduced with MC potentials. Further, a significant flexibility can be observed in SAPO-34, enhancing the diffusion of large molecules through its channel system, a behavior that is less pronounced in its siliceous counterpart.[31] We have checked that force fields used in MC and MD lead to similar results (Section S2, Supporting Information). In summary, the aim of this study is to improve models and methods so that they can describe as accurately as possible the industrially relevant process of biobutanol recovery, from the ABE fermentation, based on the combined use of several zeolite materials.

2. COMPUTATIONAL METHODOLOGY AND MODELS

2.1. MC Calculation of Adsorption Isotherms. The adsorption of butanol, ethanol, and water in ITQ-29 was investigated through adsorption isotherms. Using the ITQ-29 crystallographic structure reported by Corma et al. in 2004,[32] a 3 × 3 × 3 cell was simulated ($a = b = c = 35.6013$ Å, $\alpha = \beta = \gamma$

https://doi.org/10.1021/acs.jpcc.2c04331
J. Phys. Chem. C 2022, 126, 17680−17691

= 90.0°). Pure component and mixture adsorption isotherms were computed by the Monte Carlo method using RASPA package (version 2.0.38).[33] Simulations sampling the grand-canonical ensemble were performed during 8×10^4 initiation cycles and 5×10^5 production cycles. During the simulations, four MC moves were considered, with the same probability: adsorbates could be randomly rotated, translated, fully reinserted in the simulation box, and inserted or deleted (so-called swap move). Of these moves, "swap" starts with multiple first beads and grows the remainder of the molecule using biasing, although the explicit configurational-bias Monte Carlo move has not been used. Ewald summation method was used to handle long-range electrostatic interactions, as implemented in RASPA software. The nonbonded interactions were cut at 12.0 Å and shifted, without tail corrections. Zeolite unit cells were replicated to ensure that the simulation box size was larger than twice the cutoff distance in each direction.

The employed force field was successfully tested in similar systems previously[11,16] and has also been validated in the present study using the experimental pure component adsorption isotherms of water, ethanol, and butanol in ITQ-29[1] (further details in Section S1, Supporting Information). Butanol and ethanol were described by TRAPPE-UA (united atom) force field[34] and water molecules by TIP4P/2005.[35] Zeolite···alcohol nonbonded interactions were taken from Martin-Calvo and co-workers,[16] while zeolite···water were derived by Lorentz−Bethelot combination rules. The calculation of adsorption isotherms using Monte Carlo simulations in the grand-canonical ensemble is usually performed considering a rigid framework.[36] Such an approach significantly reduces the computational cost, enabling a larger amount of MC cycles to ensure that the equilibrium is reached and the ensemble average properties of the system are computed correctly. More importantly, we only performed the MC simulations for a pure silica material (ITQ-29), which does not present significant flexibility, hence with little impact on the adsorption properties.[36,37] Thus, the zeolite framework was kept rigid during the MC simulations, and its interaction with adsorbate molecules was considered only through zeolite oxygen atoms. Furthermore, the sodalite cages in LTA are not connected to the main zeolite channel system and were blocked during the MC simulations to prevent an overestimation of the calculated uptake.

2.2. MD Simulations. The diffusional or adsorptive behavior of water, ethanol, and butanol in ITQ-29, SSZ-13, and SAPO-34 has been assessed through MD simulations, performed with DL_POLY Classic (version 2.20).[38] All MD simulations employed the velocity Verlet integration scheme.[39] The *NVT* ensemble was sampled, with thermal control being carried out by a Nosé−Hoover thermostat.[40] A time step of 1.0 fs was used for unit cells containing silica frameworks, and a time step of 0.5 fs was used for SAPO-34 structure. SAPO materials are more flexible than, in general, silica zeolites, and the resulting larger bond elongations need to be evaluated over shorter periods of time, hence the shorter time step. The simulations were computed until the processes of interest could be captured, also taking into account the computational resources available. The initial configurations were equilibrated during 20 ps before computing the production run. During the simulations, Ewald sums were employed for the long-range Coulombic interactions, and a cutoff of 9.0 Å was applied for the van der Waals interactions. The adsorbates were modeled by the same force fields previously employed in the MC simulations (TIP4P/2005[35] for water and TRAPPE-UA for alcohol[34] molecules), whereas flexible zeolite and SAPO frameworks were described through the force field described in Ghysels et al.[41] force field, with modifications to improve the stability of AlPO and SAPO-34 structures containing surface (terminal) OH groups, discussed in detail in Section 2.5.

As illustrated by Figure 2a, all MD simulation unit cells contain two unconnected reservoirs across the crystallographic

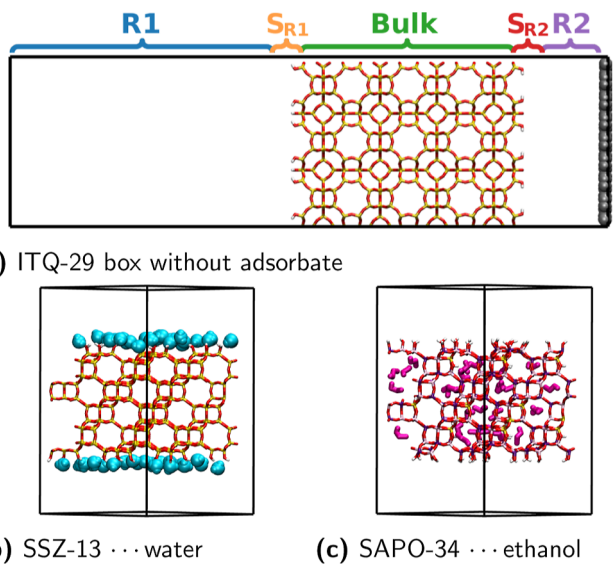

Figure 2. Example of an MD simulation unit cell without adsorbate molecules (a), where R1 and R2 are the reservoirs, S_{R1} and S_{R2} are the OH external surfaces in contact with the respective reservoirs, and the bulk region corresponds to the zeolite framework. The repulsive (or attractive) wall is depicted in gray. Example of optimized structures considered for the adsorption energy ($\overline{\Delta E^{ads}}$) calculation of molecules adsorbed in the external surface (b) or in the bulk (c).

c direction (R1 and R2, divided by an attractive or repulsive wall, depending on the simulation), and zeolite/SAPO materials were simulated by converting the bulk MC model into a nanosheet with surface OH groups at both sides facing the reservoirs. In the remaining directions (crystallographically *a*, *b*), zeolite periodicity was maintained. As the crystal lattice is flexible during the MD simulations, the SSZ-13 trigonal structure came from the IZA database ($a = b = 13.675$ Å, $c = 14.767$ Å, $\alpha = \beta = 90.0°$, $\gamma = 120.0°$).[42] Based on a $2 \times 2 \times 2$ cell, the SSZ-13 external surface was generated in the *c* crystallographic direction, leading to a nanosheet approximately 28.0 Å thick. The SAPO-34 structure was obtained from previous works.[41,43] Isolated Brønsted acid sites were included in the structure, respecting the experimental Si/Al/P molar composition reported by Dai and co-workers,[44] in which no significant numbers of Si islands are formed. A $2 \times 2 \times 2$ unit cell was generated with the chemical composition of $Si_{24}Al_{144}P_{120}O_{576}H_{24}$ and with cell parameters of $a = 27.4095$ Å, $b = 27.5039$ Å, $c = 29.5008$ Å, $\alpha = 89.9749°$, $\beta = 90.0198°$, and $\gamma = 119.8945°$ (CIF available in the Supporting Information). After the generation of the external surface, a ∼28.0 Å thick SAPO-34 nanosheet was also generated. Finally, the same crystallographic structure of ITQ-29 employed for MC calculations[32] was used in the MD simulations. Starting

https://doi.org/10.1021/acs.jpcc.2c04331
J. Phys. Chem. C 2022, 126, 17680−17691

with the 3 × 3 × 3 cell, an ITQ-29 nanosheet was constructed with a thickness of approximately 50.0 Å.

2.3. Systems to Be Simulated Using MD Resembling Biobutanol Recovery. As indicated above, process A was not simulated through MD. The dynamical behavior of ITQ-29 desorption, process B, was analyzed by the MD method. Both reservoirs were initially empty, and zeolite bulk contains the uptake obtained at the end of the Monte Carlo simulation corresponding to the adsorption of the fermented vapor mixture in ITQ-29 at 313 K. As the system evolves, ethanol and water become desorbed from ITQ-29 and occupy reservoirs R1 and R2. The simulation was performed at 393 K during 165 ns. During the experiment, the molecules that migrate from ITQ-29 bulk to the surface are removed by the stripping gas toward the second column. In order to simulate this experimental procedure, the wall that delimits R1 and R2 reservoirs was modeled with an attractive potential for the adsorbates. Therefore, when a molecule desorbs from the zeolite toward the center of the reservoirs (moves away at least 5.0 Å far from the zeolite surface), it becomes attracted by the wall, remaining in contact with it (within 2.5 Å) until the end of the simulation. This ensures that reservoirs (R1 and R2) remain almost empty, resembling the experiments using the stripping gas.

In continuation of process B, the adsorptive process C was simulated by systems containing the fully desorbed phase from ITQ-29, initially located at R1 reservoir, and exposed to either SSZ-13 or SAPO-34 (CHA) nanosheets in order to compare their relative adsorption efficiency. The aim is to observe a selective adsorption of water and ethanol in CHA, while butanol remains in the gas phase (reservoir) and can be recovered with high purity. The MD simulations run at 313 K for 250 and 200 ns, respectively.

In process C, water adsorption by CHA nanosheets is a particularly important issue. Over the computed trajectories, the water content in each region of the simulation box was calculated (based on geometrical criteria) so that the water uptake at the CHA material can be quantified. This is also done for ethanol and butanol molecules, although the first is a minor component, and only a small fraction of the latter is adsorbed. A molecule was classified as being at the zeolite surface (S_{R1} or S_{R2}) if at least a weak hydrogen bond (HB) with a silanol group was detected, whose strength could be estimated through well-established geometric criteria.[45] The selected criteria were distance between HB donor (D) and acceptor (A) closer than 4.0 Å, distance A···H ≤ 3.2 Å, and angle D−H···A at least 90° (being stronger at 180°). Consequently, the remaining molecules located inside and outside the framework composed *bulk* and *reservoir* (R1 or R2) loadings, respectively.

2.4. Summary of Calculations Performed. Along this study, it is important not only to employ an accurate force field and to design realistic models of the nanosheets resembling the experimental columns but also to integrate the different process steps so that they all describe the experimental procedure. This way, we summarize below (Table 1) all details of each calculation in order to facilitate an overall comparison to the real process.

2.5. General Force Field for Zeolite/SAPO Materials with Surface OH Groups. The general force field presented here is an extension from previous work[41,46,47] to describe flexible zeolite, AlPO, and SAPO bulk structures, as well the respective nanosheets with surface OH groups. Electrostatic

Table 1. Summary of Calculations, the Respective Experimental Process Simulated, and Employed Conditions

calculation	MC1 (Figure 3)	MD1 (Figure 4)	MD2 (Figure 5a−c)	MD3 (Figure 5d−f)
step (Figure 1)	1	2	2	2
process (Figure 1)	A	B	C	C
material	ITQ-29	ITQ-29	SSZ-13	SAPO-34
T (K)	313	393	313	313
initial	zeo is initially empty, and R1 contains the fermented vapor mixture (mix1): 0.07butanol: 0.01ethanol: 0.92 water	zeo = mix2R1 = R2 = empty	R1 = mix2R2 = empty zeo = empty	R1 = mix2R2 = emptyzeo = empty
final	zeo contains mix2: 0.71butanol: 0.01ethanol: 0.28 water	R1 + R2 containing ethanol and water; zeo containing butanol	zeo adsorbs 2.5% of butanol and 39% of the water initially contained in R1	zeo adsorbs 2.5% of butanol and 78% of the water initially contained in R1
MD time (ns)	not MD calculation	165	250	200
aim	check selective adsorption of butanol by ITQ-29	check preferential desorption of water and ethanol from ITQ-29	check preferential adsorption of water and ethanol by SSZ-13	check preferential adsorption of water and ethanol by SAPO-34

https://doi.org/10.1021/acs.jpcc.2c04331
J. Phys. Chem. C 2022, 126, 17680−17691

and van der Waals interactions were defined by the Coulomb (eq 1) and Lennard–Jones (LJ, eq 2) potential, respectively. Such parameters (Tables 2 and 3) were taken from the original works of Ghysels et al.[41] (pure silica and SAPO frameworks with Brønsted sites), and Bushuev and Sastre (surface OH charges[46] and their three-body potentials[47]). Remaining LJ parameters between surface OH and zeolite atoms were derived by Lorentz–Berthelot mixing rules. Furthermore, O–H bonds (Brønsted sites and surface groups) were described by a Morse potential (eq 3), with E_0 = 7.0525 eV, k = 2.1986 Å^{-1}, and r_0 = 0.94760 Å[41]

Table 2. Species Described by the Force Field, with Respective Atom Types and Charges (Eq 1)

species	AT	charge (e$^-$)
zeolite silicon[a]	Si	2.100
zeolite aluminum[a]	Al	1.575
zeolite phosphorus[a]	P	2.625
zeolite oxygen[a]	O2	−1.050
	O1	−0.725
zeolite Brønsted site[a]	H1	0.200
	O3	−0.950
zeolite surface hydroxyl[b]	H3	+0.425

[a]Taken from ref 42. [b]Taken from ref 47.

Table 3. LJ Parameters (Eq 2) for Intermolecular Interactions

pair	A (eV/Å^{12})	B (eV/Å^6)
Si···Si[a]	0.5601	0.0004
Si···O2[a]	172.6992	0.1086
Si···O1[a]	218.1689	0.9583
Si···O3[b]	124.1989	0.1044
Si···Al[a]	1.0153	0.0005
Si···P[a]	0.5403	0.0003
O2···O2[a]	26 877.9664	29.8306
O2···O1[a]	26 877.9664	29.8306
O2···O3[b]	27 097.4251	28.4516
O2···Al[a]	342.4165	0.0786
O2···P[a]	118.3529	0.093
O1···O1[a]	26 877.9664	29.8306
O1···O3[b]	27 097.4251	28.4516
O1···Al[a]	259.9127	0.0786
O1···P[a]	118.3529	0.093
O3···O3[c]	27 290.9346	27.1226
O3···Al[b]	236.009	0.1309
O3···P[b]	120.743	0.0908
Al···Al[a]	1.8405	0.0006
Al···P[a]	0.9794	0.0004
P···P[a]	0.5211	0.0003

[a]Taken from ref 42. [b]Derived by Lorentz–Berthelot combination rules of parameters from refs 42 and 46. [c]Taken from ref 47.

$$U^{\text{Coulomb}}(r_{ij}) = \frac{q_i q_j}{4\pi\epsilon_0 r_{ij}} \quad (1)$$

$$U^{\text{LJ}}(r_{ij}) = \left(\frac{A}{r_{ij}^{12}}\right) - \left(\frac{B}{r_{ij}^{6}}\right) \quad (2)$$

$$U^{morse}(r_{ij}) = E_0[\{1 - \exp[-k(r_{ij} - r_0)]\}^2 - 1] \quad (3)$$

When using the original parameters for SAPO frameworks with OH surface groups in the MD simulations, the flexible structure of the zeolite presented certain distortions that were absent when a completely periodic system was optimized or simulated through MD, mainly due to the removed constraints along the crystallographic c direction, where the surface was generated. These distortions were related to a significant flexibility of tetrahedral units near the surface containing Al or P centers. In the original parameterization, three-body potentials (eq 4) did not take into account the O–Al–O or O–P–O terms. However, in the less rigid nanosheet considered here, the need for those terms became evident. Therefore, in this general version of the force field, both O–Al–O and O–P–O three-body interactions were added, while the force constants (k_θ) for Si–O–Si and P–O–Al terms were properly adjusted to be consistent with the new terms (Table 4)

$$U^{\text{three-body}}(\theta_{ijk}) = k_\theta(\theta_{ijk} - \theta_0)^2 \quad (4)$$

Table 4. Three-Body Potential (Eq 4) Parameters: Force Constant (k_θ) and Equilibrium Angle (θ_0)

	new ff		old ff	
three-body	$k\theta$ (eV/rad^2)	θ_0 (deg)	$k\theta$ (eV/rad^2)	θ_0 (deg)
Ox–Si–Ox[a]	1.4944	109.470	1.4944	109.470
Ox–Al–Ox[b]	0.4747	109.470		
Oy–P–Oy[b]	0.6998	109.470		
Si–O2–Si[b]	3.1731	142.712	1.5509	142.712
Si–Oz–Al[a]	1.7875	140.831	1.7875	140.831
P–O2–Al[b]	3.8604	139.689	2.0468	139.689
H3–O3–T[c]	1.3000	100.000	1.3000	100.000

[a]Taken from ref 42. [b]This work. [c]Taken from ref 48. Generic atom types Ox (x = 1, 2, 3), Oy (y = 2, 3), Oz (z = 1, 2), and T = Si, Al, P.

For the new parameters obtained, Al and P tetrahedra are more flexible (smaller k_θ values) than the Si ones, a logic result that corresponds to the tetrahedral stability of each element.[48] It is well known that high-silica zeolites are widely employed as well due to their high hydrothermal stability[49] and that there is less thermal stability in AlPOs than in SAPO materials.[50]

In order to evaluate the capability of the new parameters to reproduce crystallographic structures, the old and new force field definitions were employed, using lattice energy minimization calculations, to obtain structural parameters of zeolites whose experimental results are available in the literature (Table 5). A fully periodic unit cell was considered, and geometry optimizations at constant pressure were performed with GULP software (version 4.3.2).[51] As summarized in Table 5, for both silica and AlPO materials, geometries optimized with the new version of the force field presented smaller deviations from the experimental unit cell parameters and volumes, when compared with the old force field. Thus, suggested modifications not only improved the accuracy of the silica and AlPO structures but also, more importantly, added generality to the force field, allowing to simulate flexibility and dynamics of silica, AlPO, and SAPO materials containing surface OH groups. This effort adds to previous studies in which the role of surface silanol groups on diffusivity and catalytic properties has been put forward,[52−57] while the role of other terminal OH groups has been suggested.[58,59]

https://doi.org/10.1021/acs.jpcc.2c04331
J. Phys. Chem. C 2022, 126, 17680−17691

Table 5. Percent of Deviation (%Δ) from Experimental Unit Cell Volume (V) and Parameters (a, b, c, α, β, and γ) in the Optimized Structures with the New and Old[41] Force Field (ff)

ff	exp. structure	% ΔV	% Δa	% Δb	% Δc	% Δα	% Δβ	% Δγ
new	AlPO-18 (1991[74])	3.6	1.6	0.8	1.1	0.0	0.0	0.0
	AlPO-34 (1985[75])[a]	3.1	1.0	1.0	1.1	0.0	0.0	0.0
	SSZ-13 (1998[76])	2.6	1.2	1.2	0.2	0.0	0.0	0.0
	ITQ-29 (2004[32])	1.7	0.6	0.6	0.6	0.0	0.0	0.0
	ITQ-29 (2012[77])	2.1	0.7	0.7	0.7	0.0	0.0	0.0
old	AlPO-18 (1991[74])	5.0	2.1	1.3	1.6	0.0	0.0	0.0
	AlPO-34(1985[75])[a]	4.5	1.4	1.4	1.6	0.0	0.0	0.0
	SSZ-13 (1998[76])	3.2	1.3	1.3	0.5	0.0	0.0	0.0
	ITQ-29 (2004[32])	2.6	0.9	0.9	0.9	0.0	0.0	0.0
	ITQ-29 (2012[77])	3.0	1.0	1.0	1.0	0.0	0.0	0.0

[a]Structure determination corresponds to $Al_4SiP_3HO_{16}{\cdot}nH_2O$.

Surface effects that can hopefully be better described by the updated force field have been long described to have a large effect on the dynamics of occluded molecules.[30,60−63] In spite of recent combined computational and experimental efforts trying to shed light on the existence of surface barriers for diffusing molecules, this is still an open question that needs further studies.[64−73]

Finally, during long MD simulations, a few occurrences of surface O−H bond breaking could be observed, caused by a strong electrostatic interaction with neighboring OH groups. The probably excessive ionic character of this H−O bond (q(O) = −0.950 e$^-$ and q(H) = 0.425 e$^-$, Table 2) was then balanced by the addition of a repulsive Buckingham potential (eq 5), applied between O···H atoms not directly bonded to each other: Ox···Hz (where x = 1, 2, 3 and z = 1,3), with A = 311.97 eV, ρ = 0.25 Å, and C = 0.0 eV Å^6. These parameters were taken from Schröder and co-workers,[78] indicating that this strategy has already been employed successfully

$$U^{\text{buck}}(r_{ij}) = A\ \exp\left(-\frac{r_{ij}}{\rho}\right) - \left(\frac{C}{r_{ij}^6}\right) \tag{5}$$

2.6. Calculation of Adsorption Energies. The bulk and surface adsorption interactions between mixture components (guests) and zeolite/SAPO frameworks were numerically estimated in terms of the average adsorption energy ($\overline{\Delta E^{\text{ads}}}$), as defined by eq 6, where $E_{\text{zeo}\cdots\text{guests}}$ is the single-point energy of zeolite···guests complex, E_{zeo} corresponds to the single-point energy of the zeolite isolated, and n_{guests} is the amount of adsorbate molecules. The single-point energy of the guests isolated (E_{guests}) is composed of their intramolecular ($E^{\text{intra}}_{\text{guests}}$) and intermolecular ($E_{\text{guest}\cdots\text{guest}}$) energy components. Thus, by subtracting only the intramolecular guest contribution in eq 6, $\overline{\Delta E^{\text{ads}}}$ will take into account both zeo···guests and guest···guest intermolecular interactions. The effect of intermolecular guest−guest interactions increases at large loading, being a large part in the adsorption energy[19]

$$\overline{\Delta E^{\text{ads}}} = \frac{E_{\text{zeo}\cdots\text{guests}} - (E_{\text{zeo}} + E^{\text{intra}}_{\text{guests}})}{n_{\text{guests}}} \tag{6}$$

Thus, for each adsorbate (butanol, ethanol, or water) and framework (ITQ-29, SSZ-13, or SAPO-34) interacting complex, a box containing water or alcohol molecules adsorbed either in the bulk or surface was simulated by the MD methodology during 10 ns. The final configuration was split into two configurations, containing the zeolite and adsorbate over the surface or bulk (as illustrated by Figure 2b,c, respectively). For each configuration, an energy minimization was performed at constant volume using GULP software and the optimized structures (Figure S9, Supporting Information) were considered in order to calculate $\overline{\Delta E^{\text{ads}}}$.

3. RESULTS AND DISCUSSION

3.1. Process (A) Adsorption of "Fermented Vapor Mixture" in ITQ-29, 313 K. Adsorption isotherms were calculated in order to obtain information about the gas mixture compositions that can be adsorbed as a function of pressure at equilibrium. According to the previous study,[1] the adsorbate pressures in the fermented vapor phase are 299 Pa of butanol, 50 Pa of ethanol, and 4220 Pa of water, giving a total pressure of 4569 Pa. By considering the mixture with molar fractions of 0.07 butanol/0.01 ethanol/0.92 water, the partial pressures simulated for each component when considering a total pressure of 4569 Pa are similar to the experimental ones: 4203.5 Pa (water), 45.7 Pa (ethanol), and 319.8 Pa (butanol). Mixtures with this composition ratio are what we call "fermented vapor mixture" (mix1, Table 1) since this is the resulting gas phase mixture from the ABE process, as described in the Introduction.

Calculated pure component isotherms of butanol and ethanol were in close agreement with experimental results (Figure 3a), which is a good validation of the models and method employed. Regarding water, the results were also in reasonable agreement, although the step at pressure above 10^3 Pa shows some disagreement with experimental results. Several force fields were tested for water, with the best results obtained with TIP4P/2005. For the selected water model, the simulation predicts more pressure than the experiment for the zeolite to start adsorbing. However, very similar effects appear with a whole series of tested potentials (Sections S1 and S2 of the Supporting Information). Various factors involving water behavior in zeolite micropores make it difficult to provide a simple and accurate modeling. For instance, the presence of defects in hydrophobic frameworks, and the changes in water dipole moment when confined in the pores, requires a more complex description[79] (with polarization and functional forms that are usually not available in the software packages), beyond our study.

Considering the fermented vapor mixture (0.07 butanol/0.01 ethanol/0.92 water and a total pressure of 4569 Pa, black line of Figure 3b), ethanol uptake is considerably low (0.015

https://doi.org/10.1021/acs.jpcc.2c04331
J. Phys. Chem. C 2022, 126, 17680−17691

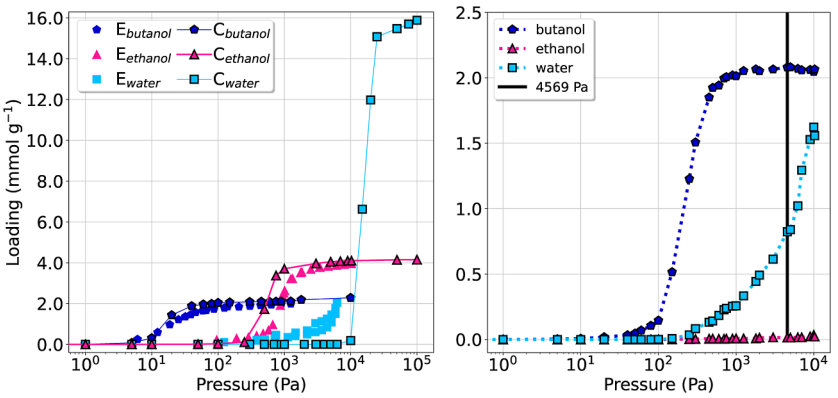

(a) pure component **(b)** mixture

Figure 3. MC1 calculation (see Table 1). (a) Experimental (E) and calculated (C) pure component (butanol, ethanol, water) adsorption isotherms in ITQ-29 at 313 K. (b) Calculated adsorption isotherms of "fermented vapor mixture" in ITQ-29 at 313 K, with the experimental pressure highlighted as a vertical black bar.

mmol·g^{-1}) as it corresponds to its relative low pressure in the initial mixture (50 Pa). The concentration of the adsorbed mixture at equilibrium is 0.71 butanol/0.01 ethanol/0.28 water, showing a butanol concentration 10 times larger than the initial mixture and a water content reduced by 70%, demonstrating that ITQ-29 structure is well suited for the butanol separation step. The higher affinity of ITQ-29 for butanol molecules is also highlighted by its $\overline{\Delta E^{ads}}$ value. The adsorption energy of butanol in the bulk is approximately 20 and 13 kJ/mol more stabilizing than those of water and ethanol, respectively (Table 6).

Table 6. Adsorption Energy ($\overline{\Delta E^{ads}}$) of Adsorbates in the Bulk or External Surface of Studied Frameworks, in kJ/mol[a]

zeolite	guest	$\overline{\Delta E^{ads}}$ (bulk)	$\overline{\Delta E^{ads}}$ (surface)
ITQ-29	butanol	−84.3	−72.0
	ethanol	−71.1	−66.7
	water	−64.6	−42.7
SSZ-13	butanol	−83.7	−77.7
	ethanol	−57.6	−66.8
	water	−45.4	−57.0
SAPO-34	butanol	−79.2	−74.7
	ethanol	−68.1	−72.2
	water	−62.6	−66.2

[a]More details in Section S5, Supporting Information.

3.2. Process (B) Selective Desorption of Water and Ethanol in ITQ-29, 393 K. Once ITQ-29 zeolite has selectively adsorbed butanol, plus water and ethanol (end of process A), the temperature is increased (from 313 to 393 K) and the desorption cycle starts (process B). The preferential desorption of water and ethanol from ITQ-29 bulk is expected from their weaker adsorption energies (Table 6). The MD simulation of ITQ-29 desorption was done using as initial geometry the final configuration from the previous (process A) MC calculation, corresponding to the adsorption of the fermented vapor mixture (Figure 4a, 81 butanol, 1 ethanol, and 32 water molecules, referred to as mix2 in Table 1).

As experimentally, due to the continuous flux of a stripping gas redirecting the desorbed molecules to the next column

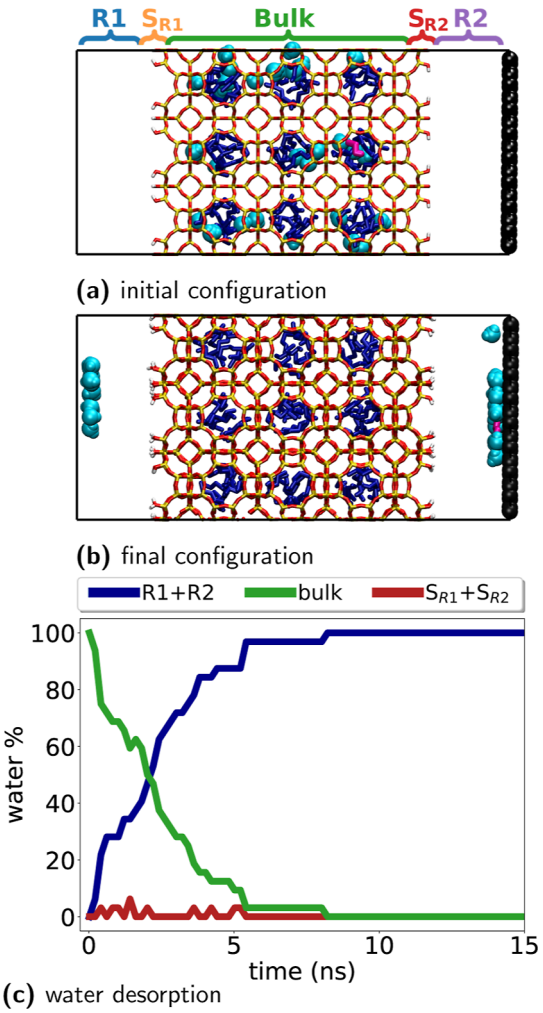

(a) initial configuration **(b)** final configuration **(c)** water desorption

Figure 4. MD1 calculation (see Table 1). Snapshots from MD simulation of vapor mixture desorption in ITQ-29 nanosheet with (a,b) attractive wall (right end of cell, in black) at 393 K. Initial configuration contains 81 butanol, 1 ethanol, and 32 water molecules adsorbed. (c) %water desorption during the simulation.

(CHA material), the equilibrium is shifted and desorption is favored. This is confirmed by the MD simulation (Figure 4b) containing an attractive wall that removes adsorbate molecules

https://doi.org/10.1021/acs.jpcc.2c04331
J. Phys. Chem. C 2022, 126, 17680−17691

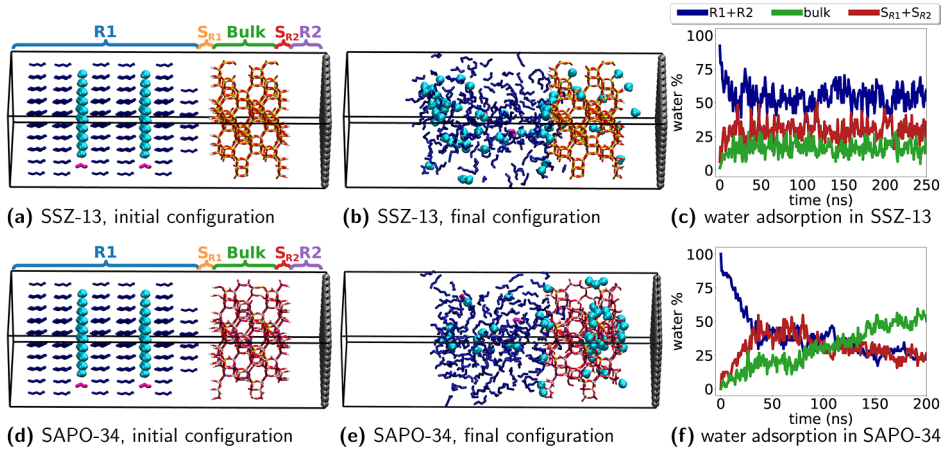

Figure 5. MD2 (top) and MD3 (bottom) calculations (see Table 1). Snapshots from MD simulations of selective adsorption of water and ethanol in SSZ-13 (a,b) and SAPO-34 (d,e) nanosheets at 313 K. In the simulations, R1 contains initially 162 butanol, 2 ethanol, and 64 water molecules. A repulsive wall (right end of the cell, in gray) separates R1 from R2. % Water adsorption over time for simulations with SSZ-13 (c) or SAPO-34 (f).

from R1 and R2 central regions. All water molecules were desorbed from ITQ-29 at 8.7 ns, and the only ethanol molecule also desorbed at 5.2 ns, while butanol molecules remained in the bulk until the end of the simulation (165 ns). This fast desorption of water and ethanol is in agreement with the experimental breakthrough curves.[1] The experimental timescale of water and ethanol desorption from ITQ-29 (50 min) is impossible to reach by the current simulation methods. However, our nanosheet is only a few nm thick, while the experimental particles are usually on the order of μm thick (×1000 factor). As a logical consequence, the desorption process could be seen in a few ns of simulation, corresponding to several minutes in the experiments. On the other hand, any butanol molecule was desorbed during the time simulated, indicating that our model is able to successfully simulate the preferential desorption of water and ethanol and that butanol desorption is a totally independent process. Furthermore, the complete desorption of butanol is a slower process due to its slow diffusion and stronger adsorption energy in ITQ-29 bulk ($\overline{\Delta E^{ads}}$ = −84.3 kJ/mol, Table 6).

3.3. Process (C) Selective Adsorption of Water and Ethanol in CHA Materials, 313 K. Simultaneously with process B, the desorbed vapor from ITQ-29 goes to the CHA material, and a second adsorption process (C) takes place. Here, the chemical composition of the second column and its affinity for ethanol and water play an important role.

In the initial configuration of the simulation boxes (Figure 5a,d), R1 contains what we call "mix2" vapor mixture (Table 1), which corresponds to the total amount of molecules adsorbed by ITQ-29, which we multiply 2 times in order to have a larger ensemble (162 butanol, 2 ethanol, and 64 water molecules). Strictly, not all butanol will be in contact with the CHA nanosheet since process (C) lasts only 50 min, and butanol molecules are released after approximately 150 min of the ITQ-29 desorption process (B).[1] However, by considering here all butanol, it will be possible to estimate, by having a larger sampling, if CHA nanosheets do really have the capacity to exclude butanol (as aimed) from the adsorbed molecules. In other words, this will be a stringent test to check how good are CHA nanosheets (SSZ-13 and SAPO-34) to selectively capture water and ethanol (Figure 5b,e).

The higher hydrophilicity of SAPO-34 material was clearly evidenced by the simulations, which reached a bulk + surface adsorption of 78% of the water molecules present after 200 ns, without still reaching equilibrium, hence suggesting that more water can be captured if the simulation is extended longer (green line of Figure 5f). Contrarily, the equilibrium could be reached after 40 ns of the simulation with SSZ-13 (green line of Figure 5c), showing a much lower performance (bulk + surface water adsorption of 39%) than SAPO-34. For both zeolites, the surface adsorption accounted for approximately 20% of the water content, being limited by the amount of terminal OH available for HB interactions. Concerning only the bulk adsorption, SAPO-34 superior adsorption of water is directly related with the larger charge separation in SAPO-34 than in silica zeolite as well as the acid sites present in the SAPO-34 structure.[80]

All ethanol and most butanol molecules were located in R1 or interacting with the surface (S_{R1}). At the end of both simulations, only 2.5% of the butanol became adsorbed in the bulk. This illustrates the slower diffusion (uptake) of butanol when compared with water molecules (Figure 5b,e), in agreement with previous experimental observations showing that butanol molecules are almost fully excluded from SAPO-34 pores.[15] On the other hand, the absence of ethanol uptake in both CHA materials is a consequence of its small fraction in the "mix2" mixture (see Table 1), and hence, no reliable data can be given for ethanol, although a behavior similar to water can be expected.

The magnitude of $\overline{\Delta E^{ads}}$ increases with the size of the molecule adsorbed on SSZ-13, SAPO-34, or ITQ-29 (butanol > ethanol > water, Table 6), according to the amount of atoms taking part in short- and long-range interactions. This trend is observed for both surface and bulk adsorption. For the smaller and more polar guests (water and ethanol), the surface adsorption at SSZ-13 and SAPO-34 leads to a greater stabilization when compared with the bulk due to the greater availability of OH groups in the surface to establish HBs, but this effect is only observed at low loading. This can be seen from the results of Table S4 if the guest−guest contribution is subtracted from the total adsorption energy, leading to values (for water in ITQ-29) of −24.4 kJ/mol (surface) and −12.0 kJ/mol (bulk). The same effect is observed for ethanol in ITQ-29. The above-mentioned preferential affinity of polar molecules, such as water, to the external surface of zeolite nanosheets has already been reported by Farzaneh and

https://doi.org/10.1021/acs.jpcc.2c04331
J. Phys. Chem. C 2022, 126, 17680−17691

collaborators for silica materials.[10] Their study highlighted that the presence of OH groups in the structure, as well as the external surface of the nanosheets, indicates regions of low selectivity for butanol as a significant content of water can be found in both regions, in particular the surface.[10] For water and ethanol in SSZ-13 and SAPO-34, this trend is also observed even at large water loadings, with values in Table 6 indicating a larger adsorption energy for water and ethanol in the surface than in the bulk. Some values in Table 6 may seem surprising, such as similar water adsorption energy in bulk ITQ-29 and SAPO-34, but this is due to the different weight of guest···guest interactions. If we only take the zeo···guest contributions (Table S4), the larger hydrophilicity of SAPO-34 leads to a stronger adsorption (−27.4 kJ/mol) than for ITQ-29 (−12.1 kJ/mol). The different loadings and contributions to the adsorption energies are more detailed in Section S5 (Supporting Information).

Owing to the difficulty to fine-tune water force fields to reproduce adsorption energies, it is convenient to compare our calculated values with experimental values as well as with other calculated values. Various experimental and simulated values for the heat of adsorption of water in SAPO-34 can be found in the literature, such as −61.8,[81,82] −60.3,[83] −65.8,[84] and −64.8[85] kJ/mol, obtained at similar loading than our calculations. Taking into account that the values of heat of adsorption differ from adsorption energies by RT ($\Delta H^{ads} = \Delta E^{ads} - RT$), which is 2.6 kJ/mol at 313 K, it can be considered that our results (ΔE^{ads} = −62.6 kJ/mol, bulk, and −66.2 kJ/mol, surface, Table 6) are in reasonable agreement with the experimentally reported.

4. CONCLUSIONS

The combination of a general force field plus computational models including zeolite frameworks with the external surface and reservoirs, mimicking nanosheets, seems to be capable of reproducing the essential behavior of the experimental process of biobutanol recovery. Since the simulations allow quantifying the results in terms of each component selectivity, this opens the way to compare computationally the performance of analogous systems by modifying not only the chemical composition of each nanosheet but also the effect of the zeolite structure by testing other frameworks. Although this cannot be done in a fast way, since the simulations are time-consuming, possible ways to speed up the calculations are underway and may allow a more systematic treatment of similar separation processes based on using multiple zeolite nanosheets and different adsorption/desorption process steps. Recent works have been reported associating machine learning models with molecular simulations as an alternative to reduce the computational cost and allow a broader exploration of the studied systems (involving different materials and types of mixtures).[86−90] For instance, Sun and co-workers combined deep neural networks and canonical Gibbs ensemble Monte Carlo simulations to study the drying process of mixtures containing 1,4-butanediol or 1,5-pentanediol in water, as well as 1,5-pentanediol and ethanol by silica MFI and LTA zeolites.[90]

From our computational study, some relations between zeolite features and process performance can be highlighted. For instance, specific silica materials with an appropriate pore size allow the selective adsorption of butanol, with impurities of ethanol and water, as well as the exclusion by size of acetone. Likewise, specific SAPO materials, highly hydrophilic, allow the selective adsorption of ethanol and water desorbed from silica material upon heating. This allows butanol of high purity to remain adsorbed in the silica material. Further heating of this material allows recovering butanol of high purity.

For the studied separation process, ITQ-29 allowed the entrance of butanol, ethanol, and water, but the larger adsorption energy of the largest molecule (butanol) allows its selective adsorption in the first step. A combination of two subsequent steps follows with an influence of the ITQ-29 desorption kinetics, leading to the faster desorption of water and ethanol, which become selectively adsorbed in the hydrophilic SAPO-34 material. Once the fast process of water and ethanol desorption from ITQ-29 and simultaneous adsorption in SAPO-34 is completed, butanol of high purity remains in ITQ-29 and can be recovered.

■ ASSOCIATED CONTENT

Supporting Information

The Supporting Information is available free of charge at https://pubs.acs.org/doi/10.1021/acs.jpcc.2c04331.

Validation of the force fields employed on Monte Carlo and MD simulations; CIF of SAPO-34 used in the calculations; further details on mixture adsorption isotherms; size and composition of MD simulation boxes; optimized geometries of adsorbate···framework complexes; and further discussion about adsorption energy calculation (PDF)

Crystallographic data of SAPO-34 (CIF)

■ AUTHOR INFORMATION

Corresponding Author

German Sastre − *Instituto de Tecnología Química, Universitat Politécnica de Valéncia, 46022 Valencia, Spain;* orcid.org/0000-0003-0496-6331; Email: gsastre@itq.upv.es

Authors

Alechania Misturini − *Instituto de Tecnología Química, Universitat Politécnica de Valéncia, 46022 Valencia, Spain;* orcid.org/0000-0002-5873-8679

Fernando Rey − *Instituto de Tecnología Química, Universitat Politécnica de Valéncia, 46022 Valencia, Spain;* orcid.org/0000-0003-3227-5669

Complete contact information is available at: https://pubs.acs.org/10.1021/acs.jpcc.2c04331

Notes

The authors declare no competing financial interest.

■ ACKNOWLEDGMENTS

This work was supported by Generalitat Valenciana (GVA) predoctoral fellowship GRISOLIAP/2019/084. We also thank GVA for PROMETEO/2021/077 project and ASIC-UPV and SGAI-CSIC for the use of computational facilities.

■ REFERENCES

(1) Van der Perre, S.; Gelin, P.; Claessens, B.; Martin-Calvo, A.; Cousin Saint Remi, J.; Duerinck, T.; Baron, G. V.; Palomino, M.; Sánchez, L. Y.; Valencia, S.; et al. Intensified Biobutanol Recovery by Using Zeolites with Complementary Selectivity. *ChemSusChem* **2017**, *10*, 2968−2977.

(2) Luque, R.; Herrero-Davila, L.; Campelo, J. M.; Clark, J. H.; Hidalgo, J. M.; Luna, D.; Marinas, J. M.; Romero, A. A. Biofuels: a Technological Perspective. *Energy Environ. Sci.* **2008**, *1*, 542−564.
(3) Huang, H.-J.; Ramaswamy, S.; Liu, Y. Separation and Purification of Biobutanol During Bioconversion of Biomass. *Sep. Purif. Technol.* **2014**, *132*, 513−540.
(4) Abdehagh, N.; Tezel, F. H.; Thibault, J. Adsorbent Screening for Biobutanol Separation by Adsorption: Kinetics, Isotherms and Competitive Effect of Other Compounds. *Adsorption* **2013**, *19*, 1263−1272.
(5) Bowen, T. C.; Vane, L. M. Ethanol, Acetic Acid, and Water Adsorption from Binary and Ternary Liquid Mixtures on High-Silica Zeolites. *Langmuir* **2006**, *22*, 3721−3727.
(6) Oudshoorn, A.; van der Wielen, L. A. M.; Straathof, A. J. J. Adsorption Equilibria of Bio-based Butanol Solutions Using Zeolite. *Biochem. Eng. J.* **2009**, *48*, 99−103.
(7) Shu, X.; Wang, X.; Kong, Q.; Gu, X.; Xu, N. High-Flux MFI Zeolite Membrane Supported on YSZ Hollow Fiber for Separation of Ethanol/Water. *Ind. Eng. Chem. Res.* **2012**, *51*, 12073−12080.
(8) Águeda, V. I.; Delgado, J. A.; Uguina, M. A.; Sotelo, J. L.; García, Á. Column Dynamics of an Adsorption−Drying−Desorption Process for Butanol Recovery From Aqueous Solutions With Silicalite Pellets. *Sep. Purif. Technol.* **2013**, *104*, 307−321.
(9) Faisal, A.; Zhou, M.; Hedlund, J.; Grahn, M. Recovery of Butanol From Model ABE Fermentation Broths Using MFI Adsorbent: A Comparison Between Traditional Beads and a Structured Adsorbent in the Form of a Film. *Adsorption* **2016**, *22*, 205−214.
(10) Farzaneh, A.; DeJaco, R. F.; Ohlin, L.; Holmgren, A.; Siepmann, J. I.; Grahn, M. Comparative Study of the Effect of Defects on Selective Adsorption of Butanol from Butanol/Water Binary Vapor Mixtures in Silicalite-1 Films. *Langmuir* **2017**, *33*, 8420−8427.
(11) Gómez-Álvarez, P.; Noya, E. G.; Lomba, E.; Valencia, S.; Pires, J. Study of Short-Chain Alcohol and Alcohol−Water Adsorption in MEL and MFI Zeolites. *Langmuir* **2018**, *34*, 12739−12750.
(12) Wu, Z.; Peng, L.; Zhang, C.; Wang, X.; Liu, H.; Wang, J.; Yan, W.; Gu, X. Extraction of Butanol From ABE Solution by MFI Zeolite Membranes. *Sep. Purif. Technol.* **2020**, *242*, 116771.
(13) Claessens, B.; Wittevrongel, G. R.; Rey, F.; Valencia, S.; Cousin-Saint-Remi, J.; Baron, G. V.; Denayer, J. F. M. Capturing Renewable Isobutanol From Model Vapor Mixtures Using an All-Silica Beta Zeolite. *Chem. Eng. J.* **2021**, *412*, 128658.
(14) Miyamoto, M.; Iwatsuka, H.; Oumi, Y.; Uemiya, S.; Van den Perre, S.; Baron, G. V.; Denayer, J. F. M. Effect of Core-Shell Structuring of Chabazite Zeolite With a Siliceous Zeolite Thin Layer on the Separation of Acetone-Butanol-Ethanol Vapor in Humid Vapor Conditions. *Chem. Eng. J.* **2019**, *363*, 292−299.
(15) Cousin Saint Remi, J.; Baron, G.; Denayer, J. Adsorptive Separations for the Recovery and Purification of Biobutanol. *Adsorption* **2012**, *18*, 367−373.
(16) Martin-Calvo, A.; Van der Perre, S.; Claessens, B.; Calero, S.; Denayer, J. F. M. Unravelling the Influence of Carbon Dioxide on the Adsorptive Recovery of Butanol from Fermentation Broth Using ITQ-29 and ZIF-8. *Phys. Chem. Chem. Phys.* **2018**, *20*, 9957−9964.
(17) Zones, S. I.Zeolite SSZ-13 and Its Method of Preparation. U.S. Patent 4,544,538 A, 1983.
(18) Keyvanloo, Z.; Nakhaei Pour, A.; Moosavi, F.; Kamali Shahri, S. M. Molecular Dynamic Simulation Studies of Adsorption and Diffusion Behaviors of Methanol and Ethanol Through ZSM-5 Zeolite. *J. Mol. Graph. Model.* **2022**, *110*, 108048.
(19) Pérez-Botella, E.; Misturini, A.; Sala, A.; Palomino, M.; Corma, A.; Sastre, G.; Valencia, S.; Rey, F. Insights into Adsorption of Linear, Monobranched, and Dibranched Alkanes on Pure Silica STW Zeolite as a Promising Material for Their Separation. *J. Phys. Chem. C* **2020**, *124*, 26821−26829.
(20) Al-Bahri, O. H. S.; Borah, B.; Elzain, M.; Varanasi, S. R. Thermodynamics of Translational and Rotational Dynamics of C9 Hydrocarbons in the Pores of Zeolite-beta. *J. Mol. Graph. Model.* **2022**, *114*, 108188.
(21) Xiong, P.; He, P.; Qu, Y.; Wang, L.; Cao, Y.; Xu, S.; Chen, J.; Ammar, M.; Li, H. The Adsorption Properties of NaY Zeolite for Separation of Ethylene Glycol and 1,2-Butanediol: Experiment and Molecular Modelling. *Green Energy Environ.* **2021**, *6*, 102−113.
(22) Guliants, V. V.; Huth, A. J. Force Fields for Classical Atomistic Simulations of Small Gas Molecules in Silicalite-1 for Energy-related Gas Separations at High Temperatures. *J. Porous Mater.* **2013**, *20*, 741−751.
(23) Krishna, R.; van Baten, J. M. Highlighting the Anti-Synergy Between Adsorption and Diffusion in Cation-Exchanged Faujasite Zeolites. *ACS Omega* **2022**, *7*, 13050−13056.
(24) Madero-Castro, R. M.; Calero, S.; Yazaydin, A. O. The Role of Hydrogen Bonding in the Dehydration of Bioalcohols in Hydrophobic Pervaporation Membranes. *J. Mol. Liq.* **2021**, *340*, 117297.
(25) Losada, I. B.; Grobas-Illobre, P.; Misturini, A.; Polaina, J.; Seminovski, Y.; Sastre, G. Separation of an Aqueous Mixture of 6-Kestose/Sucrose with Zeolites: A Molecular Dynamics Simulation. *Microporous Mesoporous Mater.* **2021**, *319*, 111031.
(26) Azizi, B.; Vessally, E.; Ahmadi, S.; Ebadi, A. G.; Azamat, J. Separation of CH_4/N_2 Gas Mixture Using MFI Zeolite Nanosheet: Insights From Molecular Dynamics Simulation. *Colloids Surf., A* **2022**, *641*, 128527.
(27) Pérez-Mendoza, M.; González, J.; Ferreiro-Rangel, C. A.; Lozinska, M. M.; Fairén-Jiménez, D.; Düren, T.; Wright, P. A.; Seaton, N. A. Pore-Network Connectivity and Molecular Sieving of Normal and Isoalkanes in the Mesoporous Silica SBA-2. *J. Phys. Chem. C* **2014**, *118*, 10183−10190.
(28) Rezlerová, E.; Zukal, A.; Čejka, J.; Siperstein, F. R.; Brennan, J. K.; Lísal, M. Adsorption and Diffusion of C1 to C4 Alkanes in Dual-Porosity Zeolites by Molecular Simulations. *Langmuir* **2017**, *33*, 11126−11137.
(29) Knio, O.; Fang, H.; Boulfelfel, S. E.; Nair, S.; Sholl, D. S. Molecular Dynamics Investigation of Surface Resistances in Zeolite Nanosheets. *J. Phys. Chem. C* **2020**, *124*, 15241−15252.
(30) Zimmermann, N. E. R.; Zabel, T. J.; Keil, F. J. Transport into Nanosheets: Diffusion Equations Put to Test. *J. Phys. Chem. C* **2013**, *117*, 7384−7390.
(31) Ferri, P.; Li, C.; Millán, R.; Martínez-Triguero, J.; Moliner, M.; Boronat, M.; Corma, A. Impact of Zeolite Framework Composition and Flexibility on Methanol-To-Olefins Selectivity: Confinement or Diffusion? *Angew. Chem., Int. Ed.* **2020**, *59*, 19708−19715.
(32) Corma, A.; Rey, F.; Rius, J.; Sabater, M. J.; Valencia, S. Supramolecular Self-assembled Molecules as Organic Directing Agent for Synthesis of Zeolites. *Nature* **2004**, *431*, 287−290.
(33) Dubbeldam, D.; Calero, S.; Ellis, D. E.; Snurr, R. Q. RASPA: Molecular Simulation Software for Adsorption and Diffusion in Flexible Nanoporous Materials. *Mol. Simul.* **2016**, *42*, 81−101.
(34) Chen, B.; Potoff, J. J.; Siepmann, J. I. Monte Carlo Calculations for Alcohols and Their Mixtures with Alkanes. Transferable Potentials for Phase Equilibria. 5. United-Atom Description of Primary, Secondary, and Tertiary Alcohols. *J. Phys. Chem. B* **2001**, *105*, 3093−3104.
(35) Abascal, J. L. F.; Vega, C. A General Purpose Model for the Condensed Phases of Water: TIP4P/2005. *J. Chem. Phys.* **2005**, *123*, 234505.
(36) Dubbeldam, D.; Walton, K. S.; Vlugt, T. J. H.; Calero, S. Design, Parameterization, and Implementation of Atomic Force Fields for Adsorption in Nanoporous Materials. *Adv. Theory Simul.* **2019**, *2*, 1900135.
(37) Vlugt, T. J. H.; Schenk, M. Influence of Framework Flexibility on the Adsorption Properties of Hydrocarbons in the Zeolite Silicalite. *J. Phys. Chem. B* **2002**, *106*, 12757−12763.
(38) Smith, W.; Forester, T. R. DL_POLY_2.0: A General-purpose Parallel Molecular Dynamics Simulation Package. *J. Mol. Graphics* **1996**, *14*, 136−141.
(39) Allen, M.; Tildesley, D.*Computer Simulation of Liquids*; Clarendon Press, 1989.

https://doi.org/10.1021/acs.jpcc.2c04331
J. Phys. Chem. C 2022, 126, 17680−17691

(40) Hoover, W. G. Canonical Dynamics: Equilibrium Phase-space Distributions. *Phys. Rev. A* **1985**, *31*, 1695−1697.
(41) Ghysels, A.; Moors, S. L. C.; Hemelsoet, K.; De Wispelaere, K.; Waroquier, M.; Sastre, G.; Van Speybroeck, V. Shape-Selective Diffusion of Olefins in 8-Ring Solid Acid Microporous Zeolites. *J. Phys. Chem. C* **2015**, *119*, 23721−23734.
(42) Framework Type CHA: International Zeolite Association database. https://europe.iza-structure.org/IZA-SC/framework.php?STC=CHA (accessed Sept 17, 2021).
(43) Sastre, G.; Lewis, D. W.; Catlow, C. R. A. Modeling of Silicon Substitution in SAPO-5 and SAPO-34 Molecular Sieves. *J. Phys. Chem. B* **1997**, *101*, 5249−5262.
(44) Dai, W.; Scheibe, M.; Li, L.; Guan, N.; Hunger, M. Effect of the Methanol-to-Olefin Conversion on the PFG NMR Self-Diffusivities of Ethane and Ethene in Large-Crystalline SAPO-34. *J. Phys. Chem. C* **2012**, *116*, 2469−2476.
(45) Gilli, G.*The Nature of the Hydrogen Bond: Outline of a Comprehensive Hydrogen Bond Theory*; Oxford University Press, 2009.
(46) Bushuev, Y. G.; Sastre, G. Atomistic Simulations of Structural Defects and Water Occluded in SSZ-74 Zeolite. *J. Phys. Chem. C* **2009**, *113*, 10877−10886.
(47) Bushuev, Y. G.; Sastre, G. Atomistic Simulation of Water Intrusion-Extrusion in ITQ-4 (IFR) and ZSM-22 (TON): The Role of Silanol Defects. *J. Phys. Chem. C* **2011**, *115*, 21942−21953.
(48) Sinha, A. K.; Sainkar, S.; Sivasanker, S. An Improved Method for the Synthesis of the Silicoaluminophosphate Molecular Sieves, SAPO-5, SAPO-11 and SAPO-31. *Microporous Mesoporous Mater.* **1999**, *31*, 321−331.
(49) Simancas, R.; Chokkalingam, A.; Elangovan, S. P.; Liu, Z.; Sano, T.; Iyoki, K.; Wakihara, T.; Okubo, T. Recent Progress in the Improvement of Hydrothermal Stability of Zeolites. *Chem. Sci.* **2021**, *12*, 7677−7695.
(50) Zanjanchi, M. A.; Ghanadzadeh, A.; Khadem-Nahvi, F. Incorporation of Silicon into AlPO-5 Framework Sites: Higher Thermal Stability and Lower Extra-Framework Aluminum Concentration. *J. Inclusion Phenom. Macrocyclic Chem.* **2002**, *42*, 295−299.
(51) Gale, J. D.; Rohl, A. L. The General Utility Lattice Program (GULP). *Mol. Simul.* **2003**, *29*, 291−341.
(52) Abril, D. M.; Slater, B.; Blanco, C. Modeling Dynamics of the External Surface of Zeolite LTA. *Microporous Mesoporous Mater.* **2009**, *123*, 268−273.
(53) Slater, B.; Titiloye, J. O.; Higgins, F. M.; Parker, S. C. Atomistic Simulation of Zeolite Surfaces. *Curr. Opin. Solid State Mater. Sci.* **2001**, *5*, 417−424.
(54) Boscoboinik, J. A.; Yu, X.; Emmez, E.; Yang, B.; Shaikhutdinov, S.; Fischer, F. D.; Sauer, J.; Freund, H.-J. Interaction of Probe Molecules with Bridging Hydroxyls of Two-Dimensional Zeolites: A Surface Science Approach. *J. Phys. Chem. C* **2013**, *117*, 13547−13556.
(55) Dib, E.; Costa, I. M.; Vayssilov, G. N.; Aleksandrov, H. A.; Mintova, S. Complex H-bonded Silanol Network in Zeolites Revealed by IR and NMR Spectroscopy Combined with DFT Calculations. *J. Mater. Chem. A* **2021**, *9*, 27347−27352.
(56) Dědeček, J.; Sklenak, S.; Li, C.; Gao, F.; Brus, J.; Zhu, Q.; Tatsumi, T. Effect of Al/Si Substitutions and Silanol Nests on the Local Geometry of Si and Al Framework Sites in Silicone-Rich Zeolites: A Combined High Resolution ^{27}Al and ^{29}Si NMR and Density Functional Theory/Molecular Mechanics Study. *J. Phys. Chem. C* **2009**, *113*, 14454−14466.
(57) Medeiros-Costa, I. C.; Dib, E.; Nesterenko, N.; Dath, J.-P.; Gilson, J.-P.; Mintova, S. Silanol Defect Engineering and Healing in Zeolites: Opportunities to Fine-tune Their Properties and Performances. *Chem. Soc. Rev.* **2021**, *50*, 11156−11179.
(58) Chizallet, C.; Raybaud, P. Pseudo-Bridging Silanols as Versatile Brønsted Acid Sites of Amorphous Aluminosilicate Surfaces. *Angew. Chem., Int. Ed.* **2009**, *48*, 2891−2893.
(59) Rey, J.; Raybaud, P.; Chizallet, C. Ab Initio Simulation of the Acid Sites at the External Surface of Zeolite Beta. *ChemCatChem* **2017**, *9*, 2176−2185.
(60) Arya, G.; Maginn, E. J.; Chang, H.-C. Effect of the Surface Energy Barrier on Sorbate Diffusion in AlPO4-5. *J. Phys. Chem. B* **2001**, *105*, 2725−2735.
(61) Zimmermann, N. E. R.; Smit, B.; Keil, F. J. On the Effects of the External Surface on the Equilibrium Transport in Zeolite Crystals. *J. Phys. Chem. C* **2010**, *114*, 300−310.
(62) Kärger, J.; Heink, W.; Pfeifer, H.; Rauscher, M.; Hoffmann, J. N.m.r. N.m.r. evidence of the existence of surface barriers on zeolite crystallites. *Zeolites* **1982**, *2*, 275−278.
(63) Whitmore, L.; Slater, B.; Catlow, C. R. A. Adsorption of Benzene at the Hydroxylated (111) External Surface of Faujasite. *Phys. Chem. Chem. Phys.* **2000**, *2*, 5354−5356.
(64) Glavatskiy, K. S.; Bhatia, S. K. Thermodynamic Resistance to Matter Flow at The Interface of a Porous Membrane. *Langmuir* **2016**, *32*, 3400−3411.
(65) Rao, S. M.; Saraçi, E.; Gläser, R.; Coppens, M.-O. Surface Barriers as Dominant Mechanism to Transport Limitations in Hierarchically Structured Catalysts − Application to the Zeolite-catalyzed Alkylation of Benzene with Ethylene. *Chem. Eng. J.* **2017**, *329*, 45−55.
(66) Thompho, S.; Chanajaree, R.; Remsungnen, T.; Hannongbua, S.; Bopp, P. A.; Fritzsche, S. The Permeation of Methane Molecules through Silicalite-1 Surfaces. *J. Phys. Chem. A* **2009**, *113*, 2004−2014.
(67) Jentys, A.; Tanaka, H.; Lercher, J. A. Surface Processes During Sorption of Aromatic Molecules on Medium Pore Zeolites. *J. Phys. Chem. B* **2005**, *109*, 2254−2261.
(68) Schnell, S. K.; Vlugt, T. J. H.; Simon, J.-M.; Bedeaux, D.; Kjelstrup, S. Thermodynamics of Small Systems Embedded in a Reservoir: a Detailed Analysis of Finite Size Effects. *Mol. Phys.* **2012**, *110*, 1069−1079.
(69) Sastre, G.; Kärger, J.; Ruthven, D. M. Diffusion Path Reversibility Confirms Symmetry of Surface Barriers. *J. Phys. Chem. C* **2019**, *123*, 19596−19601.
(70) García-Pérez, E.; Schnell, S. K.; Castillo, J. M.; Calero, S.; Kjelstrup, S.; Dubbeldam, D.; Vlugt, T. J. H. External Surface Adsorption on Silicalite-1 Zeolite Studied by Molecular Simulation. *J. Phys. Chem. C* **2011**, *115*, 15355−15360.
(71) van de Graaf, J. M.; Kapteijn, F.; Moulijn, J. A. Diffusivities of Light Alkanes in a Silicalite-1 Membrane Layer. *Microporous Mesoporous Mater.* **2000**, *35-36*, 267−281.
(72) Remi, J.; Lauerer, A.; Chmelik, C.; Vandendael, I.; Terryn, H.; Baron, G. V.; Denayer, J. F. M.; Kärger, J. The Role of Crystal Diversity in Understanding Mass Transfer in Nanoporous Materials. *Nat. Mater.* **2016**, *15*, 401−406.
(73) Sholl, D. S. A porous maze. *Nat. Chem.* **2011**, *3*, 429−430.
(74) Simmen, A.; McCusker, L. B.; Baerlocher, Ch.; Meier, W. M. The Structure Determination and Rietveld Refinement of the Aluminophosphate AlPO4-18. *Zeolites* **1991**, *11*, 654−661.
(75) Ito, M.; Shimoyama, Y.; Saito, Y.; Tsurita, Y.; Otake, M. Structure of an Aluminosilicophosphate. *Acta Crystallogr., Sect. C: Cryst. Struct. Commun.* **1985**, *41*, 1698−1700.
(76) Díaz-Cabañas, M.-J.; Barrett, A. Synthesis and Structure of Pure SiO_2 Chabazite: the SiO_2 Polymorph with the Lowest Framework Density. *Chem. Commun.* **1998**, 1881−1882.
(77) Carey, T.; Corma, A.; Rey, F.; Tang, C. C.; Hriljac, J. A.; Anderson, P. A. The Effect of Extra Framework Species on the Intrinsic Negative Thermal Expansion Property of Zeolites with the LTA Topology. *Chem. Commun.* **2012**, *48*, 5829−5831.
(78) Schröder, K.-P.; Sauer, J.; Leslie, M.; Richard, C.; Catlow, A.; Thomas, J. M. Bridging Hydrodyl Groups in Zeolitic Catalysts: a Computer Simulation of Their Structure, Vibrational Properties and Acidity in Protonated Faujasites (H−Y Zeolites). *Chem. Phys. Lett.* **1992**, *188*, 320−325.
(79) Claessens, B.; Cousin-Saint-Remi, J.; Denayer, J. F. M.Efficient Downstream Processing of Renewable Alcohols Using Zeolite Adsorbents. *New Developments in Adsorption/Separation of Small Molecules by Zeolites*; Structure and Bonding; Springer International Publishing, 2020; Vol. *184*, pp 85−119.

https://doi.org/10.1021/acs.jpcc.2c04331
J. Phys. Chem. C 2022, 126, 17680−17691

(80) Bauer, J.; Selvam, T.; Ofili, J.; Che, E.; Herrmann, R.; Schwieger, W.Stability of AlPO and SAPO molecular sieves during adsorption-desorption cycles of water vapor investigated by in-situ XRD measurements. *From Zeolites to Porous MOF Materials - The 40th Anniversary of International Zeolite Conference*; Studies in Surface Science and Catalysis; Elsevier, 2007; Vol. *170*, pp 837−844.
(81) Jänchen, J.; Stach, H.; Hellwig, U.Water Sorption in Faujasite- and Chabazite Type Zeolites of Varying Lattice Composition for Heat Storage Applications. *Zeolites and Related Materials: Trends, Targets and Challenges*; Studies in Surface Science and Catalysis; Elsevier, 2008; Vol. *174*, pp 599−602.
(82) Fasano, M.; Falciani, G.; Brancato, V.; Palomba, V.; Asinari, P.; Chiavazzo, E.; Frazzica, A. Atomistic Modelling of Water Transport and Adsorption Mechanisms in Silicoaluminophosphate for Thermal Energy Storage. *Appl. Therm. Eng.* **2019**, *160*, 114075.
(83) Kayal, S.; Baichuan, S.; Saha, B. B. Adsorption Characteristics of AQSOA Zeolites and Water for Adsorption Chillers. *Int. J. Heat Mass Transfer* **2016**, *92*, 1120−1127.
(84) Jänchen, J.; Stach, H. Shaping Adsorption Properties of Nanoporous Molecular Sieves for Solar Thermal Energy Storage and Heat Pump Applications. *Sol. Energy* **2014**, *104*, 16−18.
(85) Sun, B.; Chakraborty, A. Thermodynamic Formalism of Water Uptakes on Solid Porous Adsorbents for Adsorption Cooling Applications. *Appl. Phys. Lett.* **2014**, *104*, 201901.
(86) Deng, X.; Yang, W.; Li, S.; Liang, H.; Shi, Z.; Qiao, Z. Large-Scale Screening and Machine Learning to Predict the Computation-Ready, Experimental Metal-Organic Frameworks for CO2 Capture from Air. *Appl. Sci.* **2020**, *10*, 569.
(87) Dureckova, H.; Krykunov, M.; Aghaji, M. Z.; Woo, T. K. Robust Machine Learning Models for Predicting High CO_2 Working Capacity and CO_2/H_2 Selectivity of Gas Adsorption in Metal Organic Frameworks for Precombustion Carbon Capture. *J. Phys. Chem. C* **2019**, *123*, 4133−4139.
(88) Arora, A.; Iyer, S. S.; Hasan, M. M. F. Computational Material Screening Using Artificial Neural Networks for Adsorption Gas Separation. *J. Phys. Chem. C* **2020**, *124*, 21446−21460.
(89) Braun, E.; Zurhelle, A. F.; Thijssen, W.; Schnell, S. K.; Lin, L.-C.; Kim, J.; Thompson, J. A.; Smit, B. High-throughput Computational Screening of Nanoporous Adsorbents for CO_2 Capture from Natural Gas. *Mol. Syst. Des. Eng.* **2016**, *1*, 175−188.
(90) Sun, Y.; DeJaco, R. F.; Siepmann, J. I. Deep Neural Network Learning of Complex Binary Sorption Equilibria From Molecular Simulation Data. *Chem. Sci.* **2019**, *10*, 4377−4388.

https://doi.org/10.1021/acs.jpcc.2c04331
J. Phys. Chem. C 2022, 126, 17680−17691